

An all-optical atomic gradiometer with sub-20 fT/cm/ $\sqrt{\text{Hz}}$ sensitivity in a 22 μT earth-scale magnetic field

A. R. PERRY,^{1*} M. D. BULATOWICZ,^{2,3} M. LARSEN,³ T. G. WALKER,² AND R. WYLLIE¹

¹Georgia Tech Research Institute, Atlanta, GA 30332, USA

²University of Wisconsin–Madison, Madison, Wisconsin 53706, USA

³Northrop Grumman Systems Corporation, Woodland Hills, CA, U.S.A.

*abigail.perry@gtri.gatech.edu

Abstract: In this work we demonstrate a high sensitivity atomic gradiometer capable of operation in earth-field level environments. We apply a light-pulse sequence at four times the Larmor frequency to achieve gradiometer sensitivity $<20 \text{ fT/cm}/\sqrt{\text{Hz}}$ at the finite field strength of 22 μT . The experimental timing sequence can be tuned to the field magnitude of interest. Our one dimensional all-optical gradiometer performs a differential measurement between two regions of a single vapor cell on a 4 cm baseline. Our results pave the way for extensions to operating in higher dimensions, vector sensitivity, and more advanced gradiometers.

© 2022 Optical Society of America under the terms of the [OSA Open Access Publishing Agreement](#)

1. Introduction

Optically pumped atomic magnetometers were first demonstrated over 60 years ago [1, 2]. In its initial development, it was realized that synchronous modulation of either the magnetic field or the optical pumping dynamics provided a powerful tool for measurement. Since then, breakthroughs in sensitivity [3] have accompanied exploration of the fundamental physical limits, e.g. spin-exchange broadening suppression [4–6]. Enabling technologies like lasers and miniaturized low-power packaging have increased the fieldability of optical atomic magnetometers [7]. This has also led to applications in biomagnetic imaging [8–12], with long-term prospects in magnetic anomaly detection [13] and magnetic navigation [14]. In all of these applications a magnetic field source must be localized against a background of lower-spatial-frequency noise. Hence the measurement of magnetic field gradients, as opposed to field magnitude, is an essential enabling tool for applications. An enduring challenge is achieving high sensitivity and common-mode suppression for observing gradients with high fidelity in earth’s field [7, 15–17].

Recent work has investigated methods of spin-exchange suppression for use in earth’s-sized field by the addition of pulsed fields to modulate spin-precession [18–20] and synchronous optical pulsing [21, 22] utilizing light narrowing. Here, we show a recently demonstrated [22] synchronous light-pulse atomic magnetometer (SLAM) can be operated at high densities without excessive spin-exchange broadening of the magnetic resonance line, and extend the technique to make an inherent magnetic gradiometer. The SLAM method presumably reduces spin-exchange broadening by light-narrowing [6], in which highly polarized atoms experience reduced spin-exchange relaxation thanks to angular momentum conservation in collisions between stretched-state atoms (eg. ^{87}Rb $F = 2$, $m_F = 2$). The method works well for earth-scale fields, as demonstrated here. In the following, we report measurements of a high density two-zone SLAM with gradiometer sensitivity of $15 \text{ fT/cm}/\sqrt{\text{Hz}}$ averaged over the range of 85 Hz to 156 Hz, and shot-noise sensitivity of less than $3 \text{ fT/cm}/\sqrt{\text{Hz}}$. This sensor does not require modulating magnetic fields and is an inherent gradiometer in contrast to two magnetometer signals that are post processed for gradient measurement.

The underlying principles of our SLAM scheme can be described by an ensemble of atomic spins, polarized by a periodically pulsed, circularly-polarized pumping laser beam propagating along the axis \hat{R} . Between pump pulses, the polarized atoms precess about the external magnetic field at the Larmor frequency $\omega_L = \gamma B$, where γ is the gyromagnetic ratio. The probability of absorbing photons from the pumping laser is proportional to $(1 - P_R)$, where P_R is the component of the spin-polarization along the pump axis. If the pump repetition frequency ω is not precisely equal to ω_L , there is an enhanced absorption of photons which brings the instantaneous spin polarization closer into alignment with the light. The net result is spin precession at the pulse repetition frequency but with a phase shift ϕ between the spin-precession and the clock driving the pump pulses:

$$P_R(t) = P_\perp \cos(\omega t + \phi) + P_\parallel. \quad (1)$$

Here the component of the atomic polarization perpendicular to the external magnetic field $P_\perp = QT_2 \left(1 - (\hat{B} \cdot \hat{R})^2\right)^{1/2}$, with transverse spin relaxation time T_2 and average photon absorption rate Q . The phase shift is $\phi = \tan^{-1}(\Delta\omega T_2)$, and the frequency detuning is $\Delta\omega = \omega - \omega_L$. The parallel polarization component, P_\parallel , has a longitudinal relaxation time T_1 .

We use a co-propagating probe laser to detect the spin-polarization. The probe is detuned far off the optical resonance, $\Delta \gg \Gamma_{3/2}$, where $\Gamma_{3/2}$ is the pressure-broadened linewidth of the ^{87}Rb $5P_{3/2}$ state. Here the Faraday rotation of the light due to the spin-dependent index of refraction of the atoms is minimally perturbing [23]. This is commonly done in spin-exchange relaxation-free magnetometers [24, 25]. The probe acquires a polarization rotation

$$\theta(t) \approx NP_R(t), \quad (2)$$

where N is the number of atoms in the sample volume. Demodulation of the probe rotation angle at ω for small $\Delta\omega \approx 0$ yields in-phase and quadrature signals proportional to $NP_\perp \cos(\phi)$ and $NP_\perp \sin(\phi)$, respectively.

So far we have focused on a single co-propagating pump and probe. In practical magnetic sensing applications, there are great advantages in background noise suppression to be gained by configuring pairs or arrays of magnetometers as gradiometers or differential magnetometers [7, 15–17]. For this purpose, and especially since the Faraday rotation angles when the spins are aligned with the probe laser can be radians, it can be an advantage to send the probe light through two adjacent magnetometers so that the common mode rotation can be subtracted before converting to photocurrents. As illustrated in Figure 1(a), another output is available which measures the probe polarization rotation as it goes through both a co-propagating pump region (zone 1) and then through a counter-propagating pump region (zone 2) before polarization measurement. The total rotation in the two regions is given by

$$\delta\theta \approx N(P_{R,1}(t) - P_{R,2}(t)), \quad (3)$$

where we have assumed identical N , ω , and pump polarization in both zones. In the near resonant, small angle expansion limit where $\phi_{1,2} \ll 1$, the in-phase and quadrature demodulation of probe Faraday rotation is now sensitive to differences $N(P_{\perp,1} - P_{\perp,2})$ and $N(P_{\perp,1}\phi_1 - P_{\perp,2}\phi_2)$, respectively. Hence, the in-phase measurement is an error signal that can be used to balance the polarization in the two zones, for example by balancing the relative pump intensity. The quadrature measurement is an error signal proportional to the magnetic field gradient between the two regions when the polarization is balanced.

2. Design (experimental setup, experimental sequence)

A schematic of the experimental apparatus is shown in Figure 1(a). An isotopically enhanced ^{87}Rb atomic vapor and ≈ 300 Torr of N_2 buffer gas is housed in a rectangular pyrex cell with

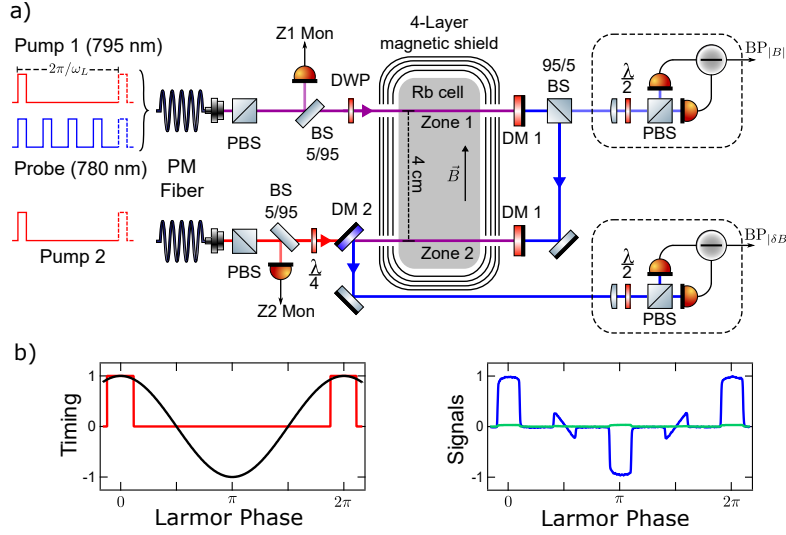


Fig. 1. SLAM configuration for the two zone, inherent gradiometer sensor. (a) Optical layout showing the two interrogation regions using a single probe beam. Red lines indicate 795 nm pump light, blue lines indicate 780 nm probe light, and purple represents co-propagating pump and probe. Optical components include Glan-Taylor polarizers (PBS), dichroic waveplate (DWP), dichroic mirrors (DM 1, DM 2), monitor photodiodes (Z1 Mon, Z2 Mon), and beam samplers (BS). (b) The once per Larmor cycle pump pulse (red), the atomic polarization along the pumping direction (black), the pulsed probe sampling of the magnetometer signal $|B|$ (blue), and the pulsed probe sampling of the gradiometer signal $|\delta B|$ (green).

inner dimensions 5 mm x 5 mm x 50 mm which is resistively heated by film heaters to an average operational temperature of ≈ 130 C, corresponding to a number density of $\approx 4 \cdot 10^{13}$ atoms/cm³. There is a ± 10 C variance between the two zones of the cell, monitored by resistance temperature detectors. The cell, thermal management, and some steering mirrors, were placed inside a 4-layer magnetic shield with integrated coils for controlling the total field and all independent magnetic field gradient components (TwinLeaf MS-2). Two measurement zones (zone 1 and 2) spaced 4 cm along the long axis of the vapor cell have independent optical pumping beams near resonant on the 795 nm D1 line with similarly-handed circular polarization, detuned ≈ 6 GHz below the un-pressure-shifted atomic value of the $5S_{1/2}, F = 1$ to $5P_{1/2}, F = 2$ transition. A probe beam detuned ≈ 40 GHz above the $5S_{1/2}, F = 2$ to $5P_{3/2}, F = 3$ transition monitors the atomic spin. All beams are collimated with a $1/e^2$ diameter ≈ 3 mm. Accounting for attenuation due to optical coatings, Rb deposits on the cell walls, and beam clipping, we estimate the time averaged probe power to be 1.6 mW in zone 1, and 890 μ W in zone 2. The time averaged pulsed pump powers are estimated to be 820 μ W in zone 1, and 1.1 mW in zone 2. This results in a photodiode detection optical power of ≈ 80 μ W in zone 1, and ≈ 520 μ W in zone 2. All parameters were empirically optimized by performing magnetic field sweeps to find the point of maximum sensitivity.

The probe and both pumps are first routed through acousto-optic modulators (AOMs), allowing independent timing and intensity control, discussed in further detail below. The probe and one pump are then combined and sent through a single polarization maintaining (PM) fiber to the experiment side optics leading to zone 1. After collimation and polarization cleanup, a dichroic waveplate rotates the linear polarized probe and circularly polarizes the co-propagating

pump. After the vapor cell, the pump is retro-reflected with a dichroic mirror, while the probe is transmitted. A pick-off mirror with balanced polarization dependence directs 5% of the transmitted probe signal to a balanced polarimeter ($BP_{|B|}$ in 1(a)), used to obtain the total field amplitude $|B|$. The probe continues to zone 2 and counter-propagates with a second pump beam of identical polarization to the first. Finally, the probe is separated by a dichroic mirror and its polarization measured by a second balanced polarimeter ($BP_{|\delta B|}$ in 1(a)), which is used to measure the magnetic field gradient. Monitor photodiodes placed in the laser beam paths of the two zones using beam samplers (BS) record the laser pulse amplitude and phases.

The left panel of Figure 1(b) shows a typical timing sequence of the 795 nm pumping laser. The pump laser is pulsed at ω_1 , which is $\omega_1 = \omega_L$ when on resonance (typical fields in this work are $22 \mu\text{T}$, $\omega_L = 2\pi \times 155 \text{ kHz}$). This sets the zero phase of the Larmor precession, with duty cycle of 10%. The atomic spin precession, $P_R(t)$, depicted in the left panel of 1(b), is monitored by the probe laser. The probe is operated either continuously or pulsed at $4\omega_L$ and the same 10% duty cycle as the pump. In the continuous probe case, the probe laser beam power is the cycle averaged optical power in the pulsed case. Typical raw signals using pulsed probing from both $BP_{|B|}$ and $BP_{|\delta B|}$ is shown in the right panel of Figure 1(b). In the pulsed case, demodulation was achieved using a fast digitizer and differencing the average signal over the $\pi/2$ and $3\pi/2$ phases for both $BP_{|B|}$ and $BP_{|\delta B|}$. Our measurements at magnetic resonance have a zero background, allowing the use of high electronic gains on the acquired signal.

Initially, experiments used a digital delay generator (SRS DG645) to control RF pulses, turning on or off the pump and probe AOMs with a measured rise time of $\approx 40 \text{ ns}$, and a separate fast digitizer (PicoScope 5444B, 125 MHz each channel). Measurements up to 0.5 seconds were made, after which the signals were digitally demodulated using one of the pump lasers as a timing reference. This experimental setup was used to acquire the data shown in Figures 2 and 3. Later measurements used FPGA firmware on a NI PXIe-5171R, a fast reconfigurable oscilloscope card with available digital outputs to gate the lasers. A digital feedback loop was implemented on the FPGA to drive the $\Delta\omega$ to zero in real time and dynamically follow a changing magnetic field. Another utility is to use this variable pulse timing to calibrate the sensitivity near resonance by sweeping the pulse timing across Larmor resonance.

3. Results

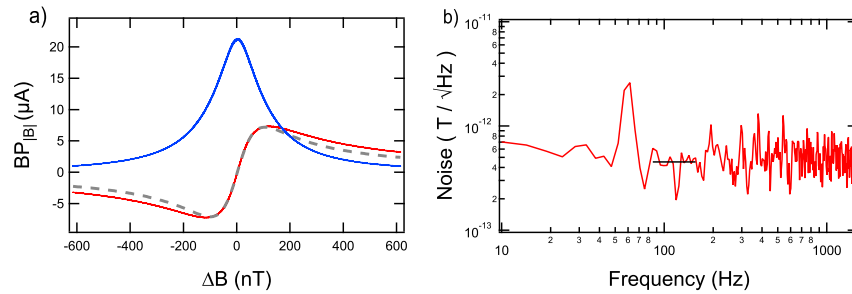


Fig. 2. Magnetic field calibration and sensitivity for a single channel SLAM magnetometer with pulsed probing (a) magnetometer magnetic field sweep across Larmor resonance at fixed pump/probe pulse timing, the blue trace show the Lorentzian amplitude response around the Larmor resonance at a phase of $0(\pi)$ in the Larmor cycle. The red (dashed gray) dispersive trace shows the derivative magnetometer response (fit) at a phase of $\pi/2(3\pi/2)$ in the Larmor cycle. (b) Magnetometer noise floor uncorrected for frequency response. The black trace is the average noise, $450 \text{ fT}/\sqrt{\text{Hz}}$, over the range 85 Hz to 156 Hz.

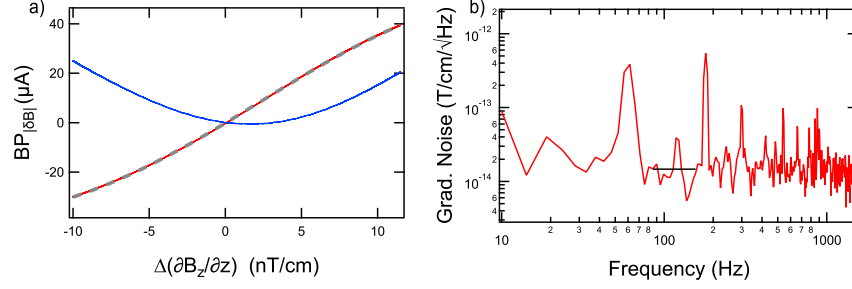


Fig. 3. Gradient magnetic field calibration and sensitivity for the SLAM magnetic gradiometer with pulsed probing (a) gradiometer magnetic field sweep for fixed pump/probe pulse timing, the blue trace shows the response of the gradiometer at phase $0(\pi)$ in the Larmor cycle when the two zone balance is offset from zero. The red dispersive feature is the gradiometer response at Larmor phase $\pi/2(3\pi/2)$ to the changing gradient, and the dotted gray trace is its fit. (b) The gradiometer noise is shown in red, and is $15 \text{ fT/cm}/\sqrt{\text{Hz}}$ averaged over the range of 85 Hz to 156 Hz shown in black.

The characterization of the pulsed pump and pulsed probe mode magnetometer and gradiometer is described below. We investigated sensor operation under a continuous probe scheme, but found the noise level to be similar to the pulsed probe case although we anticipate that the pulsed mode noise is limited by timing noise, unlike the CW mode. Further investigation is necessary to determine if the technical noise limits of the CW mode is lower than the pulsed mode. Finally, we note increased coherence times and frequency resolution has been achieved by using sub-harmonic pumping, and intend to investigate these schemes in our system in the future [26, 27].

To assess the sensitivity of the magnetometer, the magnetic field was swept across resonance by approximately $\pm 0.6 \mu\text{T}$, and we show the demodulated signals in Figure 2(a). The blue and black curves, which have nominally Lorentzian lineshape but opposite signs, are obtained from the demodulation of the magnetometer phase 0 and π probe signals, respectively. The linewidth, given by the full width at half maximum of the resulting resonance curve, is $\approx 1.4 \text{ kHz}$. The red curve is obtained by demodulating the difference between the $\pi/2$ and $3\pi/2$ probe signals. For small deviations about the bias field B_0 , the slope of the central portion of the error signal can be expressed independent of electrical gain factors by expressing the response as a ratio of the induced photocurrent from the balanced polarimeter vs the magnetic field offset from resonance, $I_{pd}/(B - B_0)$, in units of A/T. This helps make performance comparisons and scale noise measurements consistently across experiments, and is a key figure of merit in optimizing the magnetometer. This is particularly the case when it is expected that the magnetometer noise floor is dominated by the magnetic environment, rather than the fundamental limits of the sensor. Using the measured slope of the magnetometer gain, $\approx 140 \text{ A/T}$, the magnetometer noise floor is $450 \text{ fT}/\sqrt{\text{Hz}}$ shown in Figure 2(b). The magnetometer shot-noise limit is below $30 \text{ fT}/\sqrt{\text{Hz}}$.

The gradiometer signal, processed similarly to the magnetometer signal, is shown in Figure 3. The slope of the dispersion curve in Figure 3(a) gives the gradient noise calibration factor $\approx 3800 \text{ A/T/cm}$ with a magnetic gradient field sweep of approximately 15 nT/cm on either side of the magnetic resonance. The gradiometer noise was measured to be $15 \text{ fT/cm}/\sqrt{\text{Hz}}$ for the two-zone gradiometer, shown in Figure 3(b). The sensor also demonstrated gradient range of several nT/cm as seen in the magnetic field gradient sweep. During normal operation of the gradiometer, a small gradient is applied along the z -axis to bring the second zone into resonance, or balanced, with the first zone. We found that the first zone/magnetometer response changed negligibly in sensitivity at a 14 nT/cm gradient from this two-zone balance.

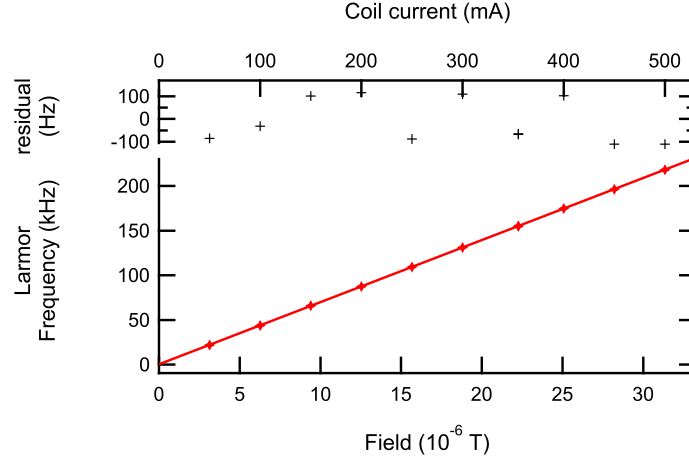


Fig. 4. Measurement of the self-oscillating mode locked frequency as a function of the magnetic field. The frequency response is linear from $\approx 3 \mu\text{T}$ to $\approx 30 \mu\text{T}$.

For sensor operation in the ambient environment, it is imperative that the sensor maintain high sensitivity while following a dynamic magnetic field environment. To this end, we have measured the timing-locked Larmor frequency as a function of applied magnetic field, shown in Figure 4. The pump pulse frequency of the magnetometer remained locked as the field was varied in the range $\approx 3 \mu\text{T}$ to $\approx 30 \mu\text{T}$. We estimate the magnitude of the quadratic Zeeman shift to be $< 50 \text{ Hz}$ across the range of the data presented, within the magnitude of the fit residuals. Implementing active pulse timing feedback control enables the magnetometer to continuously track the external field in time dynamic environments.

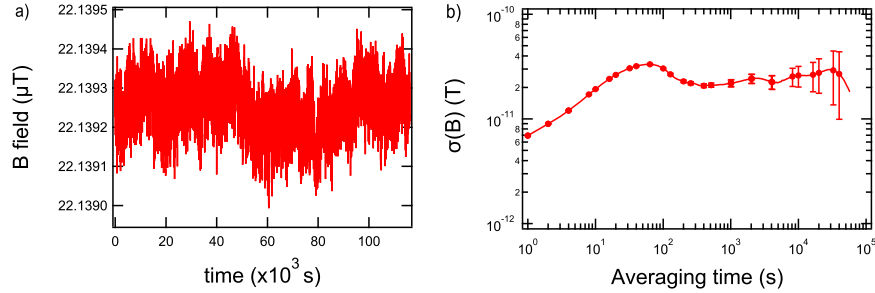


Fig. 5. (a) Long-term magnetic field measurement for the self-oscillating mode magnetometer, for a duration of 116000 sec. (b) The stability of the magnetometer signal as characterized by the total Allan Deviation.

A strength of atomic sensors is that their fundamental properties are traceable to static atomic structure. This enables applications that depend on repeated consistent measurements, e.g. magnetic surveys. If the environment can be suitably controlled, then the sensor's accuracy and sensitivity should be stable at long times. To quantify the long term behavior of our experimental apparatus, we applied a bias magnetic field using a power supply inside of a 4 layer mu-metal shield and monitored the Larmor frequency of the locked SLAM magnetometer for 116000 seconds in 1 sec averaged intervals. This measurement is shown in Figure 5(a). Figure 5(b) shows the total Allan deviation of the magnetic field (Larmor frequency) as a function of averaging time.

The stability of the system has an upper bound below 500 pT/100,000 seconds. We attribute the long term behavior to the experiment's sensitivity to both the oscillator timing drifts in the experiment control and to true magnetic field drifts, both from the active coils and attenuated fields from outside the shield.

4. Limits

Here we describe some practical limits to the SLAM measurement technique. The pulse length must be kept short compared to the Larmor period, $t_p \ll 2\pi/\omega_L$. The SLAM sensor low field limit is reached when the $2\pi/\omega_L \approx T2^*$, where spin-precession is too slow for coherent spin driving. In the present work this is approximately 0.6 μ T.

The gradient balance depends on the local polarization in each cell zone and is therefore sensitive to local pump intensity and any differential broadening mechanisms, such as probe photon absorption. While the magnetic field is measured absolutely through a frequency measurement, the gradient measurement must be calibrated. The maximum gradient that can be measured is primarily governed by the requirement that the pump pulse frequency is the same in each zone, which limited the gradient range to ± 10 nT/cm as shown in 3(a) (80 nT difference between zone 1 and zone 2).

All characterizations presented here were done with a magnetic field oriented perpendicular to the beam propagation axis, $\hat{R} \cdot \hat{B} = 0$. The technique described here, like similar Bell-Bloom demonstrations, suffers from dead zones, where response is zero when $1 - (\hat{B} \cdot \hat{R})^2 = 0$. Finally, the gradients studied here were $\partial_z B_z$. We did not investigate the dependence on gradients of other magnetic field orientations along the gradient axis.

5. Conclusion and Outlook

Here we demonstrated a two-zone synchronous light pulsed atomic magnetometer and gradiometer capable of operating in 22 μ T fields with 15 fT/cm/ $\sqrt{\text{Hz}}$ sensitivity. This method is general and many simple modifications will enable increased functionality. Presently as the angle between the external bias field and the magnetometer approaches zero the sensitivity also goes to zero creating an angular dead zone. Implementing a multi-axis magnetometer will eliminate such dead zones enabling full 3D sensing as well as vector and tensor measurements in arrays. In this earliest demonstration the pump and probe beams were recycled for use in two sensing zones. Sensitivity may be substantially enhanced by using two sets of independently tunable pump and probe beams whose power, intensity, and timing may be independently optimized for the Larmor frequency in each sensing zone. This operational concept simplifies the design of the apparatus at the cost of placing the burden of precision and complexity on the electronics: ongoing work is focused on optimization and characterization of this type of differential magnetometer [28].

Funding

This material is based upon work supported by GTRI Internal Research and Development and the Defense Advanced Research Projects Agency (DARPA) under Contract No. 140D6318C0022. The effort depicted was sponsored by the agency set forth in the schedule of the contract, and the content of the information does not necessarily reflect the position or the policy of the Government and no official endorsement should be inferred. The views, opinions and/or findings expressed are those of the author and should not be interpreted as representing the official views or policies of the Department of Defense, Department of Interior, Interior Business Center, Acquisition Services Directorate, Division III, or the U.S. Government.

Acknowledgments

We thank Gordon Morrison and Bob Buckley at Freedom Photonics for ongoing collaboration and discussions.

References

1. W. E. Bell and A. L. Bloom, "Optical detection of magnetic resonance in alkali metal vapor," *Phys. Rev.* **107**, 1559–1565 (1957).
2. W. E. Bell and A. L. Bloom, "Optically driven spin precession," *Phys. Rev. Lett.* **6**, 280–281 (1961).
3. H. B. Dang, A. C. Maloof, and M. V. Romalis, "Ultrahigh sensitivity magnetic field and magnetization measurements with an atomic magnetometer," *Appl. Phys. Lett.* **97**, 151110 (2010).
4. W. Happer and H. Tang, "Spin-exchange shift and narrowing of magnetic resonance lines in optically pumped alkali vapors," *Phys. Rev. Lett.* **31**, 273–276 (1973).
5. W. Happer and A. C. Tam, "Effect of rapid spin exchange on the magnetic-resonance spectrum of alkali vapors," *Phys. Rev. A* **16**, 1877–1891 (1977).
6. S. Appelt, A. B. A. Baranga, A. R. Young, and W. Happer, "Light narrowing of rubidium magnetic-resonance lines in high-pressure optical-pumping cells," *Phys. Rev. A - At. Mol. Opt. Phys.* **59**, 2078–2084 (1999).
7. D. Sheng, A. R. Perry, S. P. Krzyzewski, S. Geller, J. Kitching, and S. Knappe, "A microfabricated optically-pumped magnetic gradiometer," *Appl. Phys. Lett.* **110**, 031106 (2017).
8. H. Xia, A. Ben-Amar Baranga, D. Hoffman, and M. V. Romalis, "Magnetoencephalography with an atomic magnetometer," *Appl. Phys. Lett.* **89**, 211104 (2006).
9. T. H. Sander, J. Preusser, R. Mhaskar, J. Kitching, L. Trahms, and S. Knappe, "Magnetoencephalography with a chip-scale atomic magnetometer," *Biomed. Opt. Express* **3**, 981–990 (2012).
10. R. Wyllie, M. Kauer, R. T. Wakai, and T. G. Walker, "Optical magnetometer array for fetal magnetocardiography," *Opt. Lett.* **37**, 2247–2249 (2012).
11. E. Boto, S. S. Meyer, V. Shah, O. Alem, S. Knappe, P. Kruger, T. M. Fromhold, M. Lim, P. M. Glover, P. G. Morris, R. Bowtell, G. R. Barnes, and M. J. Brookes, "A new generation of magnetoencephalography: Room temperature measurements using optically-pumped magnetometers," *NeuroImage* (2017).
12. E. Boto, N. Holmes, J. Leggett, G. Roberts, V. Shah, S. S. Meyer, L. D. Muñoz, K. J. Mullinger, T. M. Tierney, S. Bestmann, G. R. Barnes, R. Bowtell, and M. J. Brookes, "Moving magnetoencephalography towards real-world applications with a wearable system," *Nature* **555**, 657–661 (2018).
13. A. Sheinker, L. Frumkis, B. Ginzburg, N. Salomonski, and B. Z. Kaplan, "Magnetic anomaly detection using a three-axis magnetometer," in *IEEE Transactions on Magnetics*, (2009).
14. A. Canciani and J. Raquet, "Absolute Positioning Using the Earth's Magnetic Anomaly Field," *Navig. J. Inst. Navig.* (2016).
15. S. J. Mullin, I. M. Savukov, G. Vasilakis, R. K. Ghosh, and M. V. Romalis, "Low-noise high-density alkali-metal scalar magnetometer," *Phys. Rev. A* **80**, 033420 (2009).
16. M. E. Limes, E. L. Foley, T. W. Kornack, S. Caliga, S. McBride, A. Braun, W. Lee, V. G. Lucivero, and M. V. Romalis, "Total-field atomic gradiometer for unshielded portable magnetoencephalography," (2020). ArXiv:2001.03534.
17. R. Zhang, R. Mhaskar, K. Smith, and M. Prouty, "Portable intrinsic gradiometer for ultra-sensitive detection of magnetic gradient in unshielded environment," (2020). ArXiv:2002.05860.
18. A. Korver, R. Wyllie, B. Lancor, and T. G. Walker, "Suppression of spin-exchange relaxation using pulsed parametric resonance," *Phys. Rev. Lett.* **111**, 043002 (2013).
19. A. Korver, D. Thrasher, M. Bulatowicz, and T. G. Walker, "Synchronous spin-exchange optical pumping," *Phys. Rev. Lett.* **115**, 253001 (2015).
20. E. Zhivun, M. Bulatowicz, A. Hryciuk, and T. Walker, "Dual-axis π -pulse magnetometer with suppressed spin-exchange relaxation," *Phys. Rev. Appl.* **11**, 034040 (2019).
21. R. Han, M. Balabas, C. Hovde, W. Li, H. M. Roig, T. Wang, A. Wickenbrock, E. Zhivun, Z. You, and D. Budker, "Is light narrowing possible with dense-vapor paraffin coated cells for atomic magnetometers?" *AIP Adv.* **7** (2017).
22. V. Gerginov, S. Krzyzewski, and S. Knappe, "Pulsed operation of a miniature scalar optically pumped magnetometer," *J. Opt. Soc. Am. B* **34**, 1429–1434 (2017).
23. W. Happer, Y. Y. Jau, and T. Walker, *Optically Pumped Atoms* (Wiley-VCH, 2010).
24. J. Allred, R. Lyman, T. Kornack, and M. Romalis, "High-sensitivity atomic magnetometer unaffected by spin-exchange relaxation," *Phys. review letters* **89**, 130801 (2002).
25. I. K. Kominis, T. W. Kornack, J. C. Allred, and M. V. Romalis, "A subfemtotesla multichannel atomic magnetometer," *Nature* **422**, 596–599 (2003).
26. G. Vasilakis, V. Shah, and M. V. Romalis, "Stroboscopic Backaction Evasion in a Dense Alkali-Metal Vapor," *Phys. Rev. Lett.* **106**, 143601 (2011).
27. V. Shah, G. Vasilakis, and M. V. Romalis, "High bandwidth atomic magnetometry with continuous quantum nondemolition measurements," *Phys. Rev. Lett.* **104** (2010).
28. M. D. Bulatowicz *et al.* (In preparation).